Optimisation of receiver's location in bender element experiments using computational wave filtration

Ionuţ Dragoş Moldovan [a],*, António Gomes Correia [b]

[a] *CERIS, Instituto Superior Técnico, Universidade de Lisboa, Lisbon, Portugal*
[b] *Institute for Sustainability and Innovation in Structural Engineering (ISISE), School of Engineering, University of Minho, Guimarães, Portugal*

A B S T R A C T

Bender elements are shear wave transducers, used for the computation of small strain shear moduli of geomaterials. However, the distortion of the output signal caused by residual compression waves may lead to important errors in the shear modulus estimates. We present a novel procedure for the optimisation of the location of the receiver bender element, to avoid regions where the distortion of the output signal is strong, without compromising the strength of the shear wave signal. The procedure is based on a computational technique naturally able to distinguish between the compression and shear waves present in the seismic response of geomaterials. This property enables the construction of compression and shear amplitude maps, that can be used to decide the best location for the receiver prior to running the experiment. The experimental validation of the procedure confirms that it leads to output signals which are easier to interpret than those obtained with the transmitter and receiver in the conventional, tip-to-tip configuration.

1. Introduction

Bender elements are piezoelectric transducers for the experimental identification of the small strain shear moduli of geomaterials. A typical experimental setup involves two bender elements inserted at opposite ends of the sample of geomaterial (Fig. 1). The controlled lateral vibration of one of the bender elements (transmitter) triggers the propagation of a shear wave through the sample, whose arrival is read by the other bender element (receiver) and converted into an electric signal, output to the user. The propagation time of the shear wave must be obtained from the input and output signals. This enables the computation of the velocity of the shear wave which, in turn, is used to derive the shear modulus.

Bender elements are a cheaper and more flexible alternative to the resonant column apparatus for shear modulus measurements. A ready-to-use bender element equipment costs far less than a resonant column, can be installed in both oedometers [1] and triaxial devices [2,3], and yields consistent measurements [4–6].

On the other hand, the interpretation of the output signal is hindered by the presence of residual compression waves, a by-product of the lateral vibration of the transmitter (Fig. 1), which may cause the output signal to be considerably different from the input signal [7,8]. Four

classes of interpretation techniques have been reported to date: (i) direct observation of the arrival time on the output signal [9]; (ii) cross-correlation of the input and output signals [10,11]; (iii) frequency domain methods [12]; and, (iv) model-based methods [7,13]. Direct observation and cross-correlation methods work with input signals compactly supported in time, typically harmonic pulses at resonant frequencies [14]. Both approaches are grounded in the assumption that the similarity between input and output signals endorses their direct comparison. However, the peak in the output signal that corresponds to the arrival of the shear wave may not be neither the first, nor the highest local maximum [7], so its accurate identification is typically quite arduous. Frequency domain approaches are used with continuous input signals. A plot with the number of wavelengths as a function of the excitation frequency is used to find the travel time [15]. The method assumes that the transformation between input and output signals is only governed by the geomechanical properties of the material, which is generally not the case due to the distortion and reflection of the travelling waves, caused by the other constituents of the testing apparatus [12]. A model-updating method for the automatic calculation of the shear modulus was recently suggested in Ref. [16]. A numerical model is created to simulate the bender element experiment, having the shear modulus as a calibration parameter. The shear modulus that maximises

---

* Corresponding author.
  E-mail addresses: dragos.moldovan@tecnico.ulisboa.pt (I.D. Moldovan), agc@civil.uminho.pt (A.G. Correia).
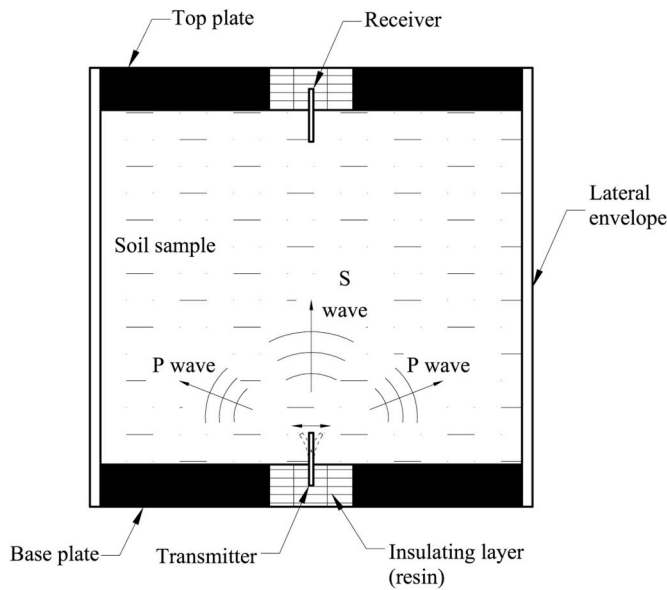
Fig. 1. Typical bender element setup.

the correlation between the output signals obtained in the lab and using the numerical model is output to the user, along with the value of that correlation, to serve as a confidence indicator.

A recent review on the performance of the bender elements for the measurement of the small strain shear modulus can be found in Ref. [17].

With the exception of the model-updating technique, all interpretation methods are strongly affected by the distortion of the output signal caused by residual compression waves [18], an effect referred to as *pollution* in the reminder of this paper. There are two sources of compression wave pollution. The most significant source is the vibration of the transmitter, which triggers not only the vertical propagation of the shear wave, but also the lateral propagation of compression waves (see Fig. 1). A secondary source of residual compression waves is the mode conversion phenomenon, implying that any type of waves reaching the lateral envelope of the sample may cause both compression and shear reflections (except for cases of critical reflection). These compression waves do travel a longer distance as they propagate laterally, but are faster than shear waves and may reach the receiver first, compromising the quality of the output signal.

While the presence of residual compression waves may be impossible to avoid, it seems reasonable to conjecture that the pollution they cause does not necessarily affect all regions of the sample equally. Indeed, on the sample's surface opposite to the transmitter there may be regions more affected by the compression wave pollution and others less so. If this is the case, then simply placing the receiver bender element in a less polluted region may help ensuring an output signal of higher quality. By *higher quality* it is meant a signal with less compression wave pollution, but still strong enough to endorse the clear reading of the shear wave.

This paper presents a novel approach for the optimisation of the receiver's location such as to avoid, to the largest extent possible, the pollution of the output signal with compression waves. Since the optimal location is problem dependent, a numerical technique for the quantification of the pollution content for a given testing setup is provided. The technique is based on the wave filtration capability of the hybrid-Trefftz finite elements [19]. As opposed to conventional (conforming) finite elements, hybrid-Trefftz elements feature approximation bases built with functions that satisfy exactly the differential equation governing the problem (the functions are combined to satisfy approximately the boundary conditions). Consequently, these functions are rich in physical information regarding the modelled phenomenon, endorsing the use of super-sized, highly convergent finite elements with relatively small

approximation bases. Moreover, the approximation functions are naturally grouped according to the type of wave they model, namely compression and shear waves in single-phase continua [20], two compression waves and a shear wave in saturated porous geomaterials [21], or three compression waves and a shear wave in unsaturated geomaterials [19]. This property opens the possibility to analyse the content of compression and shear waves throughout the sample of geomaterial, by constructing the solution using only the approximation functions associated to the desired type of wave and filtering out the others. Such analysis can be performed prior to the bender element test (using some tentative values of the shear modulus) to optimise the location of the receiver.

Hybrid-Trefftz finite elements have proved to be very well suited for modelling the highly transient wave propagation problems that typify bender element experiments. Their validation was reported in Ref. [7], followed by their application to the automatic shear modulus calculation reported in Ref. [16]. The hybrid-Trefftz elements are implemented in FreeHyTE, an open-source and user-friendly computational platform employing Trefftz methods [22,23]. This option enhances the reproducibility of this research, since FreeHyTE is freely available online [24].

A short introduction to the hybrid-Trefftz formulation for elastodynamic problems is given next, followed by the presentation of the computational filtration technique for the optimisation of the receiver's location and its validation using experimental data.

2. Numerical solution of the bender element problem

A brief description of the hybrid-Trefftz finite element models for transient wave propagation problems is given in this section. To preserve generality, the equations are cast in a form which is adequate to single-phase, saturated and unsaturated geomaterials.

2.1. Governing equations

The equation that governs the dynamic response of the geomaterial presented in Fig. 1 has the form,

$$\mathcal{D} \cdot [\boldsymbol{k}\, \mathcal{D}\, \boldsymbol{u}(\boldsymbol{x}, t)] = \boldsymbol{d} \cdot \dot{\boldsymbol{u}}(\boldsymbol{x}, t) + \boldsymbol{m} \cdot \ddot{\boldsymbol{u}}(\boldsymbol{x}, t) \tag{1}$$

where $\boldsymbol{u}(\boldsymbol{x}, t)$ is the displacement field at point $\boldsymbol{x}$ and time t, $\boldsymbol{k}$, $\boldsymbol{d}$ and $\boldsymbol{m}$ are the material stiffness, damping and mass matrices, $\dot{\boldsymbol{u}}(\boldsymbol{x}, t)$ and $\ddot{\boldsymbol{u}}(\boldsymbol{x}, t)$ are the first and second time derivatives of the displacement field, and differential operators $\mathcal{D}$ and $\mathcal{D} \cdot$ are the compatibility and equilibrium operators.

Displacement field $\boldsymbol{u}(\boldsymbol{x}, t)$ collects the displacement components in each constitutive phase of the geomaterial, namely the solid phase, for single-phase continua, the solid and fluid phases (saturated geomaterials), or solid, wetting and non-wetting fluid phases (unsaturated geomaterials). The definitions of the material stiffness, damping and mass matrices also vary according to the type of geomaterial. For multi-phase geomaterials, they are given in Ref. [25] (saturated) and [19] (unsaturated).

The following simplifying hypotheses are considered valid:

  (i) the material is (piecewise) homogeneous;
 (ii) the material has an elastic mechanical behaviour;
(iii) the displacements and strains are considered small;
(iv) the initial displacement, velocity and acceleration fields are considered null;
 (v) the problem is analysed in two dimensions (plane strain), in the oscillation plane of the bender element.

Hypotheses (i) to (iv) do not seem to be particularly problematic for the simulation of the bender element experiment, as inhomogeneous insertions can be modelled and the vibrations induced by the bender
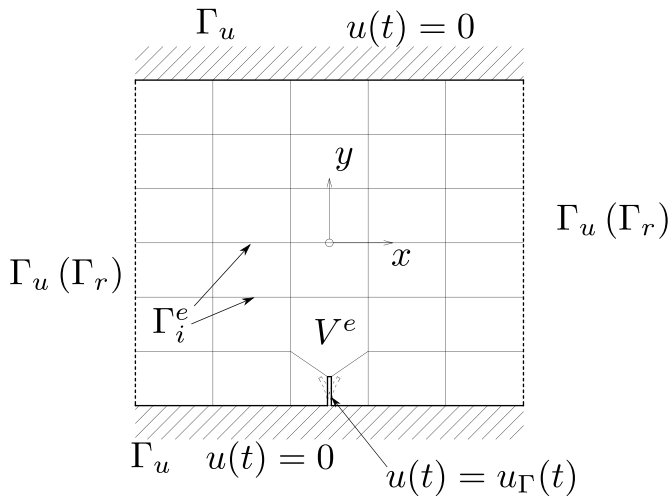
Fig. 2. Finite elements and internal boundaries.

element have very small amplitudes. Hypothesis (v) is generally incorrect, since the wave propagation induced by a bender element is inherently three-dimensional. However, the motion does take place predominantly in the vibration plane of the bender element, and past experience shows that the results obtained under the plane strain hypothesis recover sufficiently well the signal obtained in the lab [7,16]. Moreover, dealing with a plane model requires far less computational effort than using a three-dimensional model.

Domain equation (1) is complemented by the following boundary conditions:

$$u(x,t) = u_\Gamma(x,t), \quad \text{on} \ \Gamma_u \tag{2}$$

$$t(x,t) = n\,[k\,\mathcal{D}\,u(x,t)] = t_\Gamma(x,t), \quad \text{on} \ \Gamma_\sigma \tag{3}$$

$$u(x,t) + c\,t(x,t) = 0, \quad \text{on} \ \Gamma_r \tag{4}$$

where vector t collects the boundary tractions and (for multi-phase media) the pore fluid pressures, u_Γ is the displacement field prescribed on the Dirichlet boundary Γ_u, t_Γ are the tractions prescribed on the Neumann boundary Γ_σ, and n collects the components of the outward normal to the Neumann boundary. Neither the displacement nor the traction field is prescribed on elastic (Robin) boundary Γ_r. Instead, a linear relation between them is known, where c is the boundary flexibility matrix. Elastic boundary conditions can be used to simulate the presence of a flexible membrane surrounding the sample of geomaterial, or may serve as absorbing (non-reflective) boundary conditions [23].

The problem defined by equations (1)–(4) is solved in two steps. In the first step, the original equations in time and space are reduced to a series of problems in space (time discretization). In the second step, each of these time-discretized problems is solved using the hybrid-Trefftz finite element method. The solution procedure is described in the following sections.

2.2. Time discretization

The time discretization of equations (1)–(4) is performed using a weighted residual approach described in detail in Ref. [26]. The time variation of the unknown (displacement, velocity, acceleration and traction) fields is approximated as,

$$u(x,t) = \sum_{n=1}^{N} W_n(t)u_n(x) \tag{5}$$

$$v(x,t) = \sum_{n=1}^{N} W_n(t)v_n(x) \tag{6}$$

$$a(x,t) = \sum_{n=1}^{N} W_n(t)a_n(x) \tag{7}$$

$$t(x,t) = \sum_{n=1}^{N} W_n(t)t_n(x) \tag{8}$$

where $W_n(t)$ is the generic term of the time basis and N is its dimension. No restrictions besides completeness and linear independence are enacted on the time basis. In FreeHyTE, a Daubechies wavelet basis is used, to enhance the convergence and robustness of the results and to enable the use of a single time step in all analyses.

The same basis is used to enforce all domain equations, including the velocity and acceleration definitions, which are not implicitly observed because of the independent approximation of the respective weights,

$$\int_0^{\Delta t} W^*(v - \dot{u})\,dt = 0 \tag{9}$$

$$\int_0^{\Delta t} W^*(a - \dot{v})\,dt = 0 \tag{10}$$

$$\int_0^{\Delta t} W^*[\mathcal{D}{\cdot}(k\,\mathcal{D}\,u) - d{\cdot}\dot{u} - m{\cdot}\ddot{u}]\,dt = 0 \tag{11}$$

where Δt is the time step and W^* denotes the conjugate transposed of basis W.

The procedure detailed in Ref. [26] is applied to equations (9)–(11) to reduce them to a series of spectral equations in space, of type,

$$\mathcal{D}{\cdot}[k\mathcal{D}u_n(x)] + \omega_n^2\,\rho_n u_n(x) = 0 \tag{12}$$

where ω_n is an algorithmic frequency, depending on the time basis and complex, in general,

$$\rho_n = m - \frac{\hat{\imath}}{\omega_n}d \tag{13}$$

and $\hat{\imath}$ is the imaginary unit.

The similar enforcement of the boundary conditions (2) to (4) yields,

$$u_n(x) = u_{\Gamma_n}(x), \quad \text{on} \ \Gamma_u \tag{14}$$

$$t_n(x) = n\,[k\,\mathcal{D}\,u_n(x)] = t_{\Gamma_n}(x), \quad \text{on} \ \Gamma_\sigma \tag{15}$$

$$u_n(x) + c\,t_n(x) = 0, \quad \text{on} \ \Gamma_r \tag{16}$$

where u_{Γ_n} and t_{Γ_n} are the projections of the prescribed boundary conditions onto the functional space defined by basis W. It is noted that none of the fields present in the spectral problems defined by equations (12)–(16) has particular physical meanings.

The solutions of the spectral problems are obtained using the hybrid-Trefftz finite element method, as shown in the next section. The index n designating the current spectral problem is dropped from this point on, to keep notations simple.

2.3. Hybrid-Trefftz finite elements

Let the domain presented in Fig. 1 be discretized into finite elements and let V^e denote the domain of a finite element and Γ_i^e the internal boundaries between adjacent finite elements (Fig. 2). Besides internal boundaries, exterior finite elements may also have Dirichlet (Γ_u^e), Neumann (Γ_σ^e) or Robin (Γ_r^e) boundaries.

The displacement model of the hybrid-Trefftz finite element formulation is based on the independent approximations of the displacement

Table 1
Physical properties of Toyoura sand.

Property	Value
Specific gravity	2.65
Initial void ratio	0.688
Maximum void ratio	0.928
Minimum void ratio	0.677
Effective grain size, $D_{10}(mm)$	0.12
Mean grain size, $D_{50}(mm)$	0.18
Coefficient of uniformity	1.43

field in the domain of the element and of the traction field on its essential boundary, $\Gamma_e^e = \Gamma_u^e \cup \Gamma_r^e \cup \Gamma_i^e$, reading, respectively,

$$u = Up, \quad \text{in } V^e \tag{17}$$

$$t = Zq, \quad \text{on } \Gamma_e^e \tag{18}$$

where U and Z are the displacement and traction approximation bases and p and q are their unknown weights.

The essential feature of the hybrid-Trefftz finite elements is that the approximation basis in the domain of the element is constructed using trial functions that satisfy exactly the differential equation governing the problem. This means that basis U is constrained to satisfy exactly equation (12),

$$\mathcal{D} \cdot (k \, \mathcal{D}U) + \omega^2 \rho \, U = 0 \tag{19}$$

The expressions of the terms in equation (19) depend on the type of material (single-phase, saturated or unsaturated). In all cases, however, the equation is solved by applying the Helmholtz decomposition

principle. The displacement functions U are defined as the irrotational and solenoidal components of some potential functions φ_P and φ_S,

$$U = [\nabla \varphi_P \quad \widetilde{\nabla} \varphi_S \qquad \qquad] \tag{20}$$

where subscripts P and S designate the type of wave (compression and shear, respectively), ∇ is the gradient operator and $\widetilde{\nabla}$ is the curl operator.

Substitution of these potentials in equation (19) reduces it to a series of uncoupled Helmholtz equations of type,

$$\nabla^2 \varphi_j + \beta_j^2 \varphi_j = 0 \tag{21}$$

where ∇^2 is the Laplace operator, $j = \{P, S\}$, and β_j is a complex wave number. The solutions of the Helmholtz equation in two dimensions and using a polar referential (r, θ) are given by,

$$\varphi_j(r, \theta) = J_m(\beta_j r) \exp(\widehat{i} m \theta) \tag{22}$$

where $J_m(\beta_j r)$ is the Bessel function of the first kind and integer order m.

Regardless of the type of material, a single wave number (β_S) is obtained for the shear wave. Conversely, the number of compression wave numbers (β_P) that satisfy equation (19) is equal to the number of phases of the material. Therefore, the layout of the Trefftz basis features more than one block of compression waves for multi-phase media. For biphasic (saturated) materials, it is,

$$U = \left[\underbrace{\nabla \varphi_{P_1} \quad \nabla \varphi_{P_2}}_{\text{P waves}} \quad \underbrace{\widetilde{\nabla} \varphi_S}_{\text{S wave}} \right] \tag{23}$$
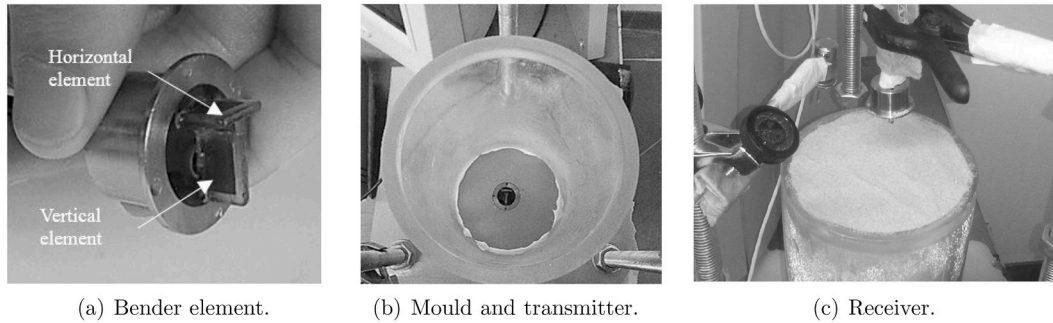

(a) Bender element.　　(b) Mould and transmitter.　　(c) Receiver.

Fig. 3. Experimental setup.

Fig. 4. Finite element mesh and applied excitation.

(a) $G_0 = 5\text{MPa}$.

(b) $G_0 = 10\text{MPa}$.

(c) $G_0 = 15\text{MPa}$.

(d) $G_0 = 20\text{MPa}$.

Fig. 5. Time-histories of horizontal displacements at the tip of the receiver. The blue dots mark the end of the sampling window. (For interpretation of the references to colour in this figure legend, the reader is referred to the Web version of this article.)

while for triphasic (unsaturated) materials, it reads,

$$U = \left[\underbrace{\nabla\varphi_{P_1} \quad \nabla\varphi_{P_2} \quad \nabla\varphi_{P_3}}_{\text{P waves}} \quad \underbrace{\widetilde{\nabla}\varphi_S}_{\text{S wave}} \right] \tag{24}$$
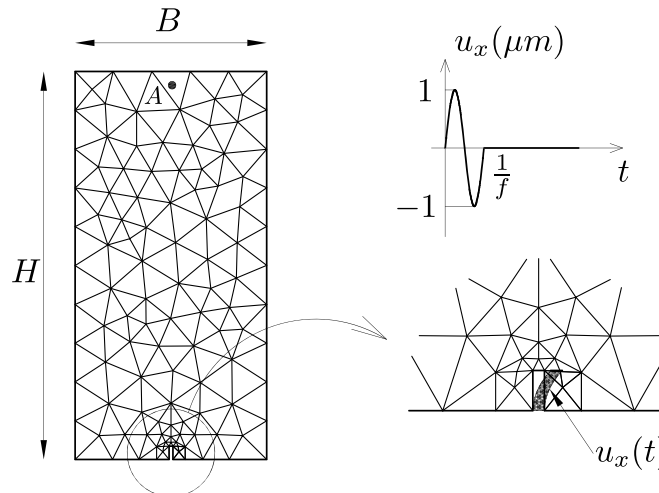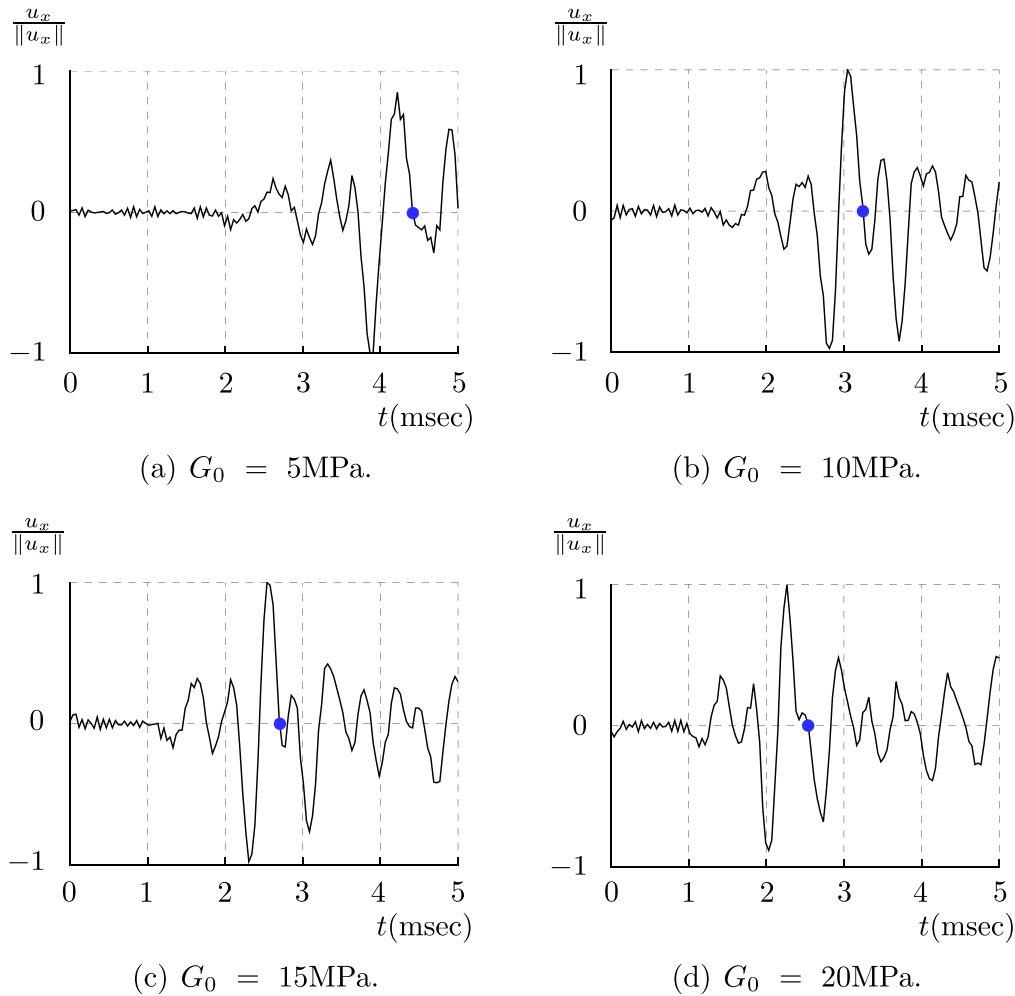
Further details on the exact expressions of the displacement bases can be found in Refs. [19–21], for single-phase, saturated and unsaturated materials, respectively.

Expressions (20), (23) and (24) show that the domain bases feature a clear distinction between the approximation functions corresponding to each type of wave. This property is exploited for the computational wave filtration, as shown in the next section.

Unlike domain basis, no particular constraints are enforced on the boundary basis Z, which is constructed in FreeHyTE using Chebyshev polynomials. All bases are hierarchical (so the addition of new functions does not call for the redefinition of the existing functions) and not connected in any way to the nodes of the elements (as typical to conventional finite elements).

After the definition of the approximation bases, equations (12), (14) and (16) are enforced weakly, using bases U and Z for weighting. The process, presented in detail in Refs. [19–21], leads to the following definition for the finite element solving system:

$$\begin{bmatrix} D & -B \\ -B^* & -C \end{bmatrix} \begin{pmatrix} p \\ q \end{pmatrix} = \begin{pmatrix} \bar{t}_\Gamma \\ -\bar{u}_\Gamma \end{pmatrix} \tag{25}$$

where,

$$D = \int U^* \, n \, (k\mathcal{D}U) \, d\Gamma^e \tag{26}$$

$$B = \int U^* \, Z \, d\Gamma_e^e \tag{27}$$

$$C = \int Z^* \, c \, Z \, d\Gamma_r^e \tag{28}$$

$$\bar{t}_\Gamma = \int U^* \, t_\Gamma \, d\Gamma_\sigma^e \tag{29}$$

$$\bar{u}_\Gamma = \int Z^* \, u_\Gamma \, d\Gamma_u^e \tag{30}$$

In the above expressions, Γ^e designates the total boundary of the element, block C is null on all boundaries except Γ_r^e, and vector $\bar{u}_\Gamma$ is null on all boundaries except Γ_u^e.

The solution of system (25) enables the construction of the generalised displacement field u for each spectral problem, using approximation (17). After all spectral problems are solved, the solution in time is recovered using approximation (5).

3. Optimisation of the receiver's location

The numerical model presented above is used to quantify the

(a) $\text{Tr}_P, G_0 = 5\text{MPa}.$ (b) $\text{Tr}_P, G_0 = 10\text{MPa}.$ (c) $\text{Tr}_P, G_0 = 15\text{MPa}.$ (d) $\text{Tr}_P, G_0 = 20\text{MPa}.$

(e) $\text{Tr}_S, G_0 = 5\text{MPa}.$ (f) $\text{Tr}_S, G_0 = 10\text{MPa}.$ (g) $\text{Tr}_S, G_0 = 15\text{MPa}.$ (h) $\text{Tr}_S, G_0 = 20\text{MPa}.$

(i) $u_{max}, G_0 = 5\text{MPa}.$ (j) $u_{max}, G_0 = 10\text{MPa}.$ (k) $u_{max}, G_0 = 15\text{MPa}.$ (l) $u_{max}, G_0 = 20\text{MPa}.$
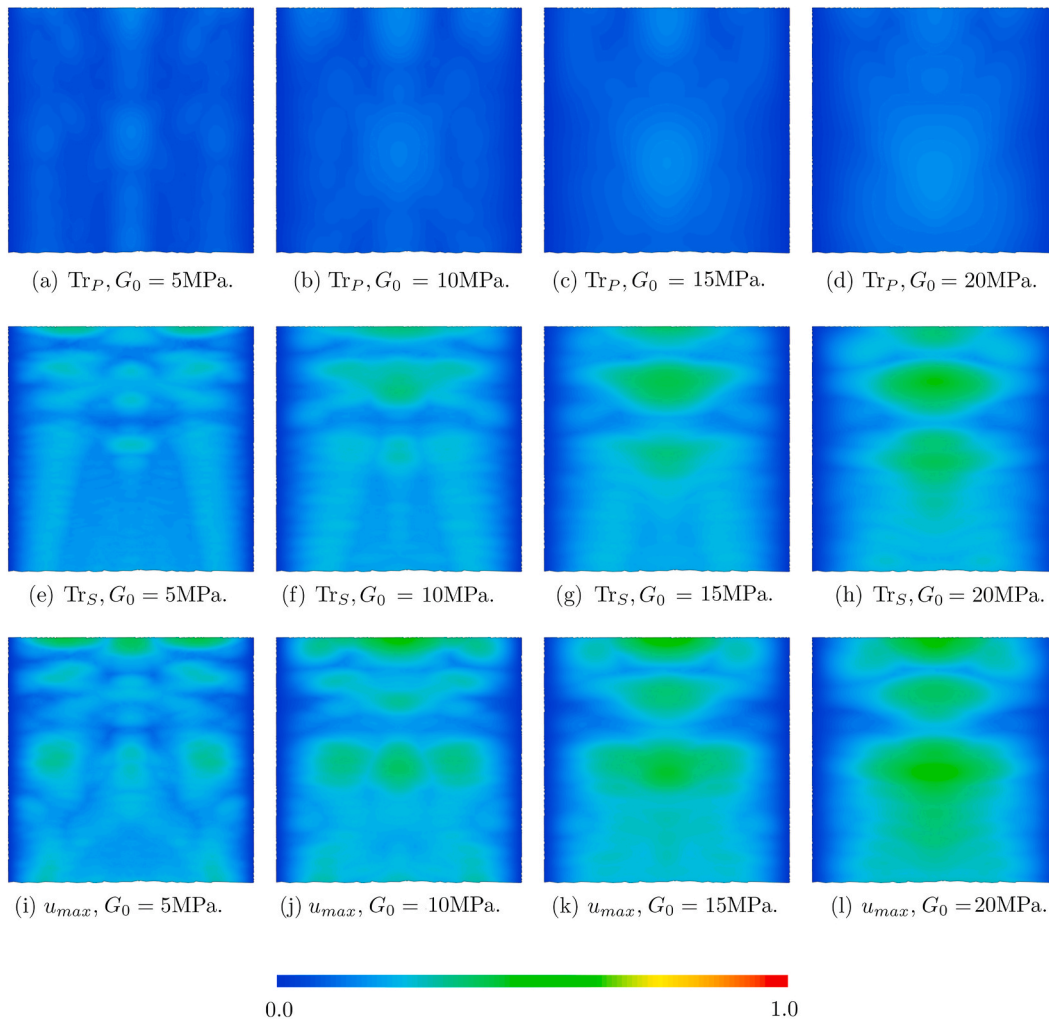
0.0   1.0

Fig. 6. Compression and shear traces and normalised displacement amplitudes.

intensity of the compression wave pollution near the top of the sample and to identify (problem-dependent) 'optimal' locations for the receiver bender element. A general procedure to do so is given next.

3.1. Compression and shear traces

The natural capability of the hybrid-Trefftz finite elements to discern between the types of waves entering the response of the sample is exploited to assess how the sample is affected by the propagation of the compression waves. The solution vector $\boldsymbol{p}$ obtained from system (25) collects the weights associated to the displacement functions in bases (20), (23) or (24), and is thus structured according to the type of wave the respective function corresponds to. Without recalculating the finite element solution, the undesired types of waves are filtered out in the post-processing by artificially setting their weights to zero.

In order to acquire a global perspective over how some subdomain $\widetilde{V}$ of the sample V is affected by the compression (shear) waves, the compression (shear) trace at a point of the sample is defined as the maximum absolute value of the horizontal displacement at that point, caused by the compression (shear) waves from the start of the experiment until some moment t_a where the arrival of the shear wave to the receiver is considered to be certain (the sampling window, $t \in [0, t_a]$),

$$\text{Tr}_P(\boldsymbol{x}) = \max_{0 \le t \le t_a} \| u_{x_P}(\boldsymbol{x}, t) \| \tag{31}$$

$$\text{Tr}_S(\boldsymbol{x}) = \max_{0 \le t \le t_a} \| u_{x_S}(\boldsymbol{x}, t) \| \tag{32}$$

where u_{x_P} and u_{x_S} are the horizontal displacements computed by setting to zero the weights corresponding to the shear and compression functions, respectively, and $\boldsymbol{x} \in \widetilde{V}$. The displacement field used to compute the compression and shear traces should be taken in the direction where the receiver is vibrating. For simplicity, it is assumed that this is the horizontal direction (as is the case in Fig. 1).

Traces (31) and (32) offer considerable insight into the compression wave pollution and shear wave strength, enabling the identification of the "optimal" location for the receiver, according to the procedure detailed in the next section.

3.2. General optimisation procedure

A general optimisation procedure for the location of the receiver bender element consists of the following steps.

Step 1. Choose a range of plausible values for the small strain shear modulus, G_0.

The uncertainty regarding the shear modulus is the most significant threat to the success of this procedure. However, past experience and a basic knowledge on the type of geomaterial should be sufficient to choose a variation interval for the shear modulus, $G_0 \in [G_0^{min}, G_0^{max}]$. In the limit, a conventional bender element test, with the transmitter and receiver in a tip-to-tip configuration can be performed and the shear modulus range can be assessed based on its results. In practice, however,
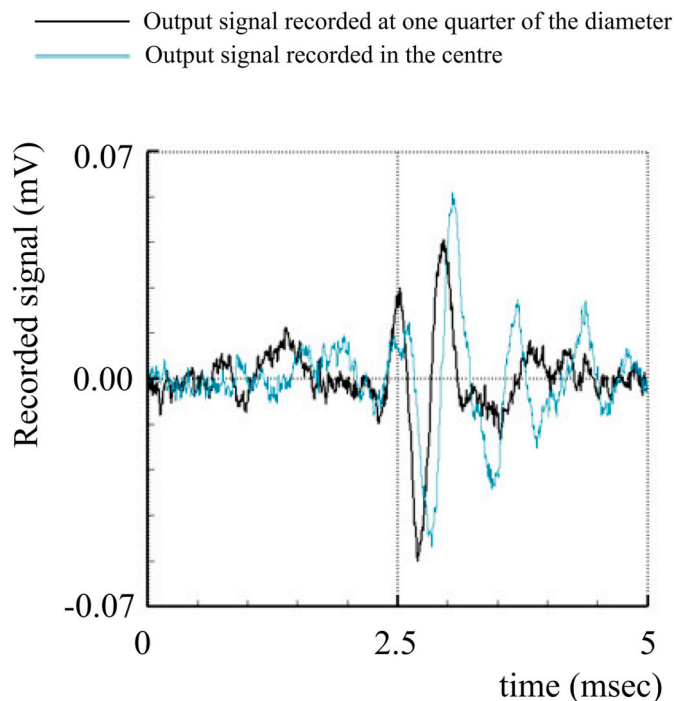
—————— Output signal recorded at one quarter of the diameter
—————— Output signal recorded in the centre

Fig. 7. Output signals recorded at two receiver locations.

this is rarely needed, as the optimal location of the receiver is fairly robust to uncertainty, as shown in the next section.

Step 2. Build hybrid-Trefftz finite element models for a number of shear moduli in the range chosen in Step 1 and obtain their solutions.

The full solution, including all types of waves should be obtained at this stage. The solution should be checked for convergence and compliance with the enforced boundary conditions. Note that the stress continuity is not enforced on the interior boundaries of the mesh, so a continuous stress field is a good convergence indicator.

Step 3. Using the solutions obtained in Step 2, plot the time-history of the horizontal displacement in the point corresponding to the tip of the receiver in its conventional (tip-to-tip) configuration and select the sampling window.

Since we are mainly interested in the arrival time of the shear wave, the response of the medium after the wave arrives is not particularly relevant. This means that the sampling window only needs to span the time until the arrival of the shear wave. It is recommended that it starts at the onset of the experiment and ends after the first large oscillation in the output signal. The first large oscillation is easy to identify in the output signal and occurs during or after the arrival of the shear wave.

Step 4. For each finite element model analysed in Step 2, construct the compression and shear traces using the sampling window adopted in Step 3.

The compression and shear traces are constructed using definitions (31) and (32), respectively, and plotted in the region where the receiver bender element will be inserted. Since the traces are meant to reflect the behaviour of the medium *before* the insertion of the receiver, the latter is not explicitly included in the model. This renders the compression and shear traces independent of the final position chosen for the receiver, and simplify the numerical model by avoiding the need of complex coupling conditions at the interface between piezoelectric and porous materials.

It is recalled that the computation of the traces does not require the recomputation of the finite element solution. Instead, wave filtration only requires setting to zero the weights of the approximation functions that need to be filtered out from bases (20), (23) or (24).

Step 5. Analyse the maps of the compression and shear traces obtained in Step 4 and choose an adequate location for the receiver.

The 'optimal' location for the receiver should ensure that the compression wave pollution is limited, and the intensity of the shear wave is still strong enough to enable its clear identification.

This procedure is illustrated for a practical situation in the next section.

4. Application and validation

The procedure for the optimisation of the receiver's location presented in the previous sections is used here for a practical situation.

A particularly striking evidence of the uncertainty involved in the interpretation of bender element experiments was provided by an international parallel test on the measurement of small strain shear moduli conducted between 2003 and 2006 by the International Society of Soil Mechanics and Geotechnical Engineering. Similar samples of a poorly-graded Toyoura sand were shipped to 23 laboratories (from 11 countries), which were asked to measure the small strain shear moduli of the samples under different confining pressures. Then, the results coming from the laboratories were centralised, analysed and published [27]. The interpretation uncertainty was larger at low confining pressures, where the average shear modulus was less than two times its standard deviation. This is the case analysed in this section.

4.1. Experimental setup

The experimental setup is fully described in Ref. [7]. The sample of dry Toyoura sand with the geomechanical properties listed in Table 1 is prepared using the dry tamping method and poured in a cylindrical acrylic mould with a height of 200 mm and diameter of 100 mm. The rigid lateral walls of the mould provide confinement for the sample. No additional confinement pressure is applied.

Two bender elements (Fig. 3(a)) were inserted at the opposite ends of the sample, the transmitter in the centre of the bottom plate (Fig. 3(b)) and the receiver in a customisable position at the top of the sample (Fig. 3(c)). The shear wave is triggered by the lateral vibration of the transmitter. A sinusoidal pulse with a 2.0 kHz frequency is applied to the sample.

4.2. Numerical setup

The numerical model is constructed using the hybrid-Trefftz finite element platform FreeHyTE [22]. The domain with $H = 200$mm and $B = 100$mm is meshed using 198 hybrid-Trefftz finite elements, as shown in Fig. 4. The mesh refinement is increased in the vicinity of the transmitter, to enhance the capacity of the model to recover the large field gradients present in that region. The dimensions of the finite elements near the transmitter range between 2 mm and 7 mm, with the former dimension conditioned by the width of the transmitter. Further away from the transmitter, however, the size of the elements increase rapidly. The leading dimension of the finite elements outside the refined zone is roughly 20 mm. This size is quite considerable if compared to the restriction typically enforced on conventional (conforming) finite elements, where at least six (but preferably 10) finite elements per wavelength are recommended. Indeed, for the excitation frequencies tested in this paper, the wavelengths of the shear waves range between 18 mm and 75 mm, and the wavelengths of the secondary compression waves are roughly one order of magnitude less. Hybrid-Trefftz finite elements are much less wavelength-sensitive than their conventional counterparts
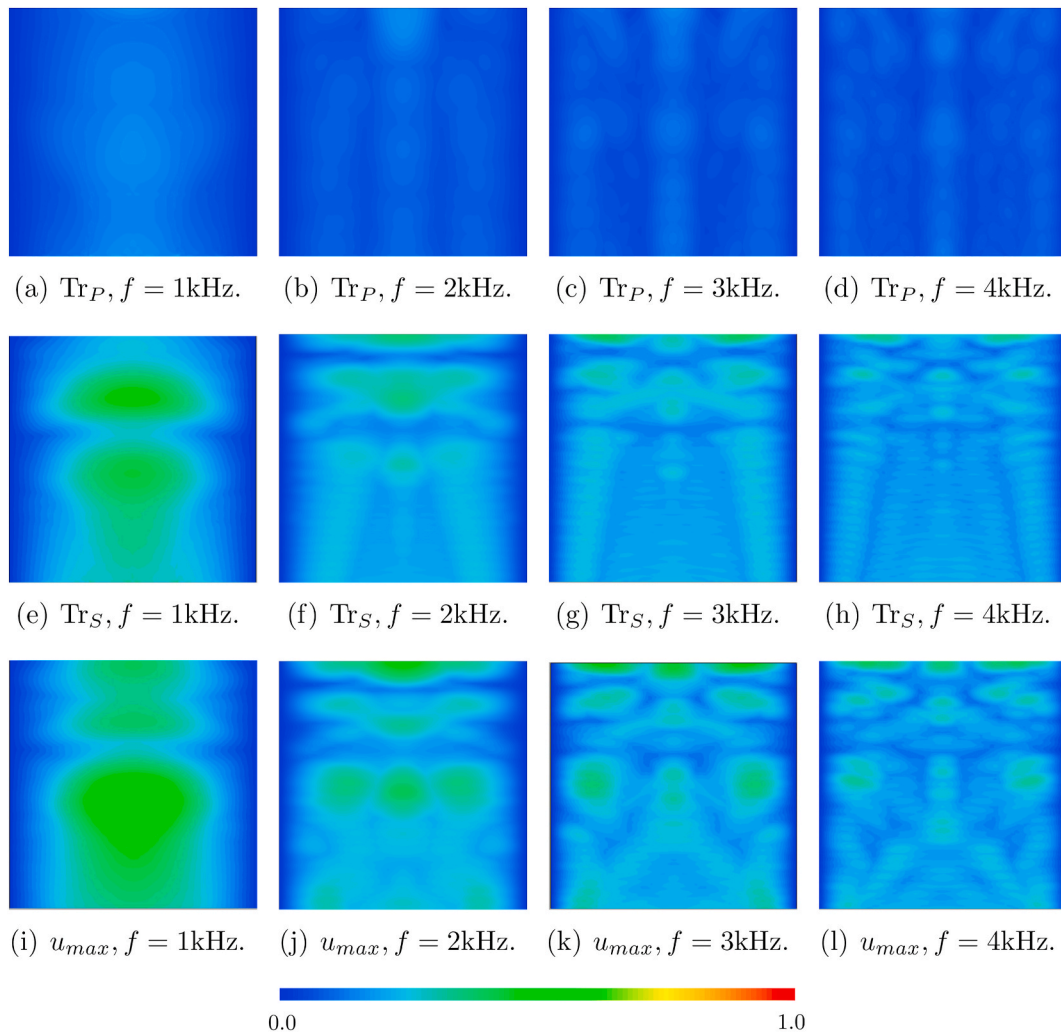
(a) $\mathrm{Tr}_P, f = 1\mathrm{kHz}.$ (b) $\mathrm{Tr}_P, f = 2\mathrm{kHz}.$ (c) $\mathrm{Tr}_P, f = 3\mathrm{kHz}.$ (d) $\mathrm{Tr}_P, f = 4\mathrm{kHz}.$

(e) $\mathrm{Tr}_S, f = 1\mathrm{kHz}.$ (f) $\mathrm{Tr}_S, f = 2\mathrm{kHz}.$ (g) $\mathrm{Tr}_S, f = 3\mathrm{kHz}.$ (h) $\mathrm{Tr}_S, f = 4\mathrm{kHz}.$

(i) $u_{max}, f = 1\mathrm{kHz}.$ (j) $u_{max}, f = 2\mathrm{kHz}.$ (k) $u_{max}, f = 3\mathrm{kHz}.$ (l) $u_{max}, f = 4\mathrm{kHz}.$

0.0   1.0

Fig. 8. Compression and shear traces and normalised displacement amplitudes.

due to their frequency-dependent approximation bases that contain considerable physical insight on the problem that is being solved [19].

The dry Toyoura sand is modelled as a porous medium saturated with air, under plane strain conditions. Its behaviour is governed by the Biot's theory of porous media [28]. The formulation is based on the $u - w$ variant of the Biot's theory, where the displacements in the solid phase and the fluid seepage are the primary variables. This variant, implemented by default in FreeHyTE, is more general than the alternative $u - p$ formulation (where pore pressure is the primary fluid variable instead of seepage), as it does not neglect the seepage acceleration. It is noted that modelling porous media as single-phase continua may lead to gross errors if the relative displacement between solid and fluid phases is significant, as it often happens in permeable geomaterials [29,30].

The exterior boundaries of the mesh are of Dirichlet type, except for the top boundary, which is defined as Neumann. All Dirichlet boundaries are considered frictionless, so the tangential displacements are unconstrained. The boundary-normal displacements are fully restricted on all Dirichlet boundaries, except the three boundaries where the sample is in contact with the transmitter. On these boundaries, a cantilever-type horizontal displacement is enforced, as shown in the detail in Fig. 4, in order to model the triggering motion of the bender element. The total insertion length of the bender element is 7 mm. The time variation $u_x(t)$ of the lateral motion of the transmitter corresponds to a 2.0 kHz sine pulse with a 1μm amplitude, as shown in Fig. 4. On the top boundary of the mesh, the stresses and pore pressure are assumed null at all times. The total time of the analysis is set to 5msec.

4.3. Shear and compression traces

The general optimisation procedure presented above is applied to improve the location of the receiver bender element.

Step 1 of the optimisation procedure involves the selection of an interval of plausible values for the small strain shear modulus. Based on previous experience with this type of material, and taking into account that no additional confining pressure is applied besides that provided by the lateral walls of the container, the shear modulus is expected to be inferior to 20 MPa.

In Step 2, four finite element models are built for shear moduli in the interval $G_0 \in [5, 20]$MPa, namely using $G_0 = 5$MPa, $G_0 = 10$MPa, $G_0 = 15$MPa and $G_0 = 20$MPa. The receiver bender element is not included in the models, but the time-histories of the horizontal displacements are recorded at its tip, in point $A(50, 193)$mm. The time-histories for each tested shear modulus, normalised to the respective maximum absolute value, are plotted in Fig. 5.

The plots are used to estimate the sampling window needed to produce the compression and shear traces in Step 4. As advised in the description of the procedure, the sampling window starts at $t = 0$msec and ends after the first large oscillation in the output signal. The end-points are marked with blue dots in the plots.

Colour plots of the compression (31) and shear (32) traces in the upper half of the sample ($100mm \leq y \leq 200mm$) for the four shear moduli are presented in Fig. 6. For comparison, the colour plot of the horizontal displacement amplitude,
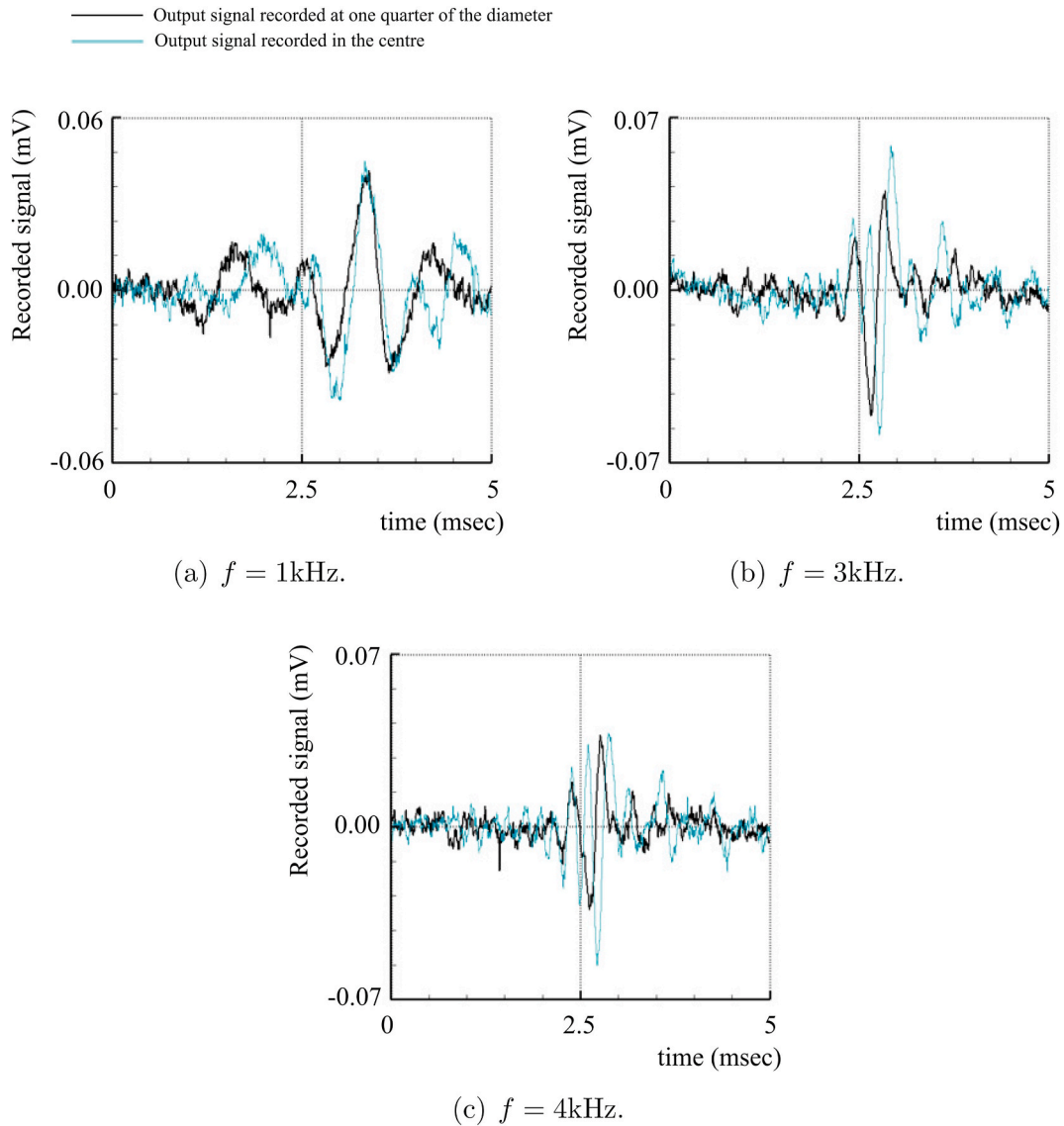
(a) $f = 1\text{kHz}$.

(b) $f = 3\text{kHz}$.

(c) $f = 4\text{kHz}$.

Fig. 9. Output signals recorded at two receiver locations for three excitation frequencies.

$$u_{max}(\boldsymbol{x}) = \max_{0 \leq t \leq t_a} \|u_x(\boldsymbol{x}, t)\| \qquad (33)$$

obtained by considering all types of waves, is also presented for each case. All displacements are normalised to the displacement amplitude of the tip of the transmitter.

The plots clearly show that shear waves (second row in Fig. 6) are more important to the response of the sample than compression waves (top row in the same figure). The amplitudes of the compression and shear traces measured at the top surface of the sample do not change much for the different shear moduli. The maximum compression traces at the top of the sample are comprised between 13% and 16% of the displacement amplitude at the tip of the transmitter. The maximum shear traces at the top of the sample are comprised between 33% and 35% of the displacement amplitude of the tip of the transmitter. The ratio between the amplitudes of the compression and shear waves at the top of the sample is a pollution indicator. It varies between 0.38 for $G_0 = 20\text{MPa}$ and 0.48 for $G_0 = 5\text{MPa}$, meaning that the compression wave pollution is also quite stable for all cases.

In spite of the higher intensity of the shear trace, compression waves still cause a significant effect on the amplitude of the displacement field (third row in Fig. 6). This can be seen comparing the Tr_S and u_{max} plots. The presence of the compression waves upsets the regular patterns of the

shear traces and significantly more irregular fields are obtained for u_{max}. It is recalled that $u_{max} \neq \text{Tr}_P + \text{Tr}_S$ because of the absolute values in definitions (31) to (33).

Conversely, compression traces are fairly regular. For low values of the shear modulus, they present three neat higher intensity zones near the top of the sample, one in the centre of the sample and the other two symmetric in respect to the vertical axis of the recipient. For the highest shear modulus, the high intensity zones move closer to the centre of the sample and become slightly more diffuse. The ratios between the compression traces at one quarter of the diameter and in the centre are 0.5, 0.63, 0.56 and 0.83 for the four shear moduli. The loci of the high intensity compression traces correspond to areas where the cross-propagating compression waves are reflected (from the lateral envelope of the sample) or combine with one another, increasing their intensity in the process.

Shear traces exhibit a similar pattern. For the lowest shear modulus, the maximum shear intensity is not even recorded in the centre of the sample, but at roughly a quarter of the diameter. For the 10 MPa shear modulus, the shear trace is distributed diffusely over a large zone of the top surface of the sample, becoming more concentrated towards the centre as the shear modulus increases. The ratios between the shear traces at one quarter of the diameter and in the centre are 1.42, 0.80,

0.62 and 0.63 for the four shear moduli.

4.4. Optimisation of receiver's location and experimental validation

The positioning of the receiver bender element at the top of the sample is considerably flexible. This was demonstrated by the in-plane directivity measurements reported in Ref. [14], which proved that the strength of the received signal is not compromised by the collocation of the receiver with an offset in respect to the standard, tip-to-tip configuration. On the contrary, the highest peak amplitude of the output signal was recorded in a slightly unaligned configuration. The results presented above are in line with these findings. The shear wave presents a fairly homogeneous intensity at the top of the sample, from the centre until close to the lateral walls, especially for the lower shear moduli.

The location of the receiver should be chosen such as to mitigate the effect of the polluting compression waves, while not compromising the intensity of the shear waves. Therefore, a good position for the receiver seems to be in the zone situated between the central and lateral higher intensity compression traces. While the locations of the higher intensity zones depend on the assumed shear modulus, it seems that positioning the receiver at one quarter of the diameter may be a good practical option for all cases.

The testing setup described above is used to run bender element experiments with receivers located in the centre of the sample (for reference) and at one quarter of the diameter. The comparison between the output signals recorded in the centre and at one quarter of the sample's diameter are presented in Fig. 7.

The first arrival is identified using the automatic procedure presented in Ref. [16] at 2.5msec, which corresponds to a shear modulus $G_0 = 9.77$MPa, which stands within the range assumed in Step 1.

This presentation focuses on the impact of the receiver's location on the ease of (visual) interpretation of the resulting output signal. In terms of the amplitude of the output signal, shifting the receiver out of the centre does not seem to cause significant losses. The main difference between the signals concerns, however, the sharpness of the amplitude corresponding to the first arrival, around 2.5msec. While the arrival signal recorded in the centre presents an M-shaped pattern spread along the time axis, the arrival recorded at one quarter of the diameter is characterised by a clear, sharp peak instead. This feature enables the clear identification of the arrival time, simplifying the visual interpretation of the output signal.

While the conclusions regarding the optimal location of the receiver element are obviously problem-dependent, the underlying causes of the formation of a compression band in the central axis of the sample should remain valid if the lateral walls of the recipient reflect the incoming compression waves back into the sample. Therefore, the installation of a receiver bender element away from the centre of the sample should definitely be considered, either as a stand-alone measuring device or in conjunction with another, central receiver.

4.5. Extension to other excitation frequencies

While the main purpose of this paper is to describe and validate the procedure for the optimisation of the location of the receiver bender element, it is probably of interest to assess to which extent the optimal location of the receiver is affected by the frequency of the pulse excitation induced by the transmitter. It is widely accepted that the excitation frequency should be chosen close to the resonant frequency of the coupled bender-soil system [31]. However, this resonant frequency is not easy to evaluate precisely because the stiffness of the geomaterial is not known in advance, so it is a common practice to run the experiments using various excitation frequencies. In the example presented here, the resonant frequency is expected to be around 2 kHz, but it seems reasonable to experiment with pulses between 1 kHz and 4 kHz.

To assess how the optimal location of the receiver is affected by the variations of the excitation frequency, numerical models are constructed using the 'exact' shear modulus, $G_0 = 9.77$MPa and pulse frequencies of 1 kHz, 2 kHz, 3 kHz and 4 kHz. The models are ran once again to obtain the compression, shear and maximum displacement traces for each frequency, which are presented in Fig. 8. The values of the traces are normalised to the displacement amplitude of the tip of the transmitter.

Most of the comments made for the displacement traces in Fig. 6 remain valid for the three higher frequencies. The compression traces in Fig. 8(b)–8(d) present three neat higher intensity bands, one in the centre of the sample and the other two symmetric in respect to the vertical axis of the recipient. The compression bands away from the centre get closer to the side walls of the recipient as the excitation frequency increases. For the low frequency configuration (Fig. 8(a)), the lateral compression bands are too close to the centre to distinguish them from the axial band. Their blending causes the axial band to be wider than for higher frequency cases. Shear traces also exhibit three higher intensity bands for the three higher frequencies (Figures 8(f) to8(h)), leaning towards the central axis. Conversely, for the lowest frequency, the bands are conjoined in the centre of the sample.

Based on the plots in Fig. 8, it seems that the location of the receiver at one quarter of the diameter, deemed adequate for the 2 kHz frequency (see the previous section), is also an adequate choice for the higher frequencies (3 kHz and 4 kHz). Indeed, such location would avoid the higher compression bands in Fig. 8(b)–8(d) while remaining in the high shear zones in Fig. 8(f)–8(h). The placement of the receiver outside the centre of the sample is more problematic for the lower frequency case, as the bulk of the compression and shear traces occupy the same locus in the sample and it does not seem to be possible to find a zone where the former is dim while the latter is strong.

These conclusions are validated empirically by repeating the lab experiments presented in the previous section, with frequencies ranging from 1 to 4 kHz. Again, two receivers are used, one in the centre of the sample (for reference) and the other at one quarter of the diameter. The comparison between the respective output signals are presented in Fig. 9 (a)–9(c). The signal obtained for the 2 kHz frequency case is presented in Fig. 7.

The experiments confirm the forecast of the numerical models. For the higher frequencies, the amplitude of the shear wave arrival, recorded around 2.5msec, is much clearer when the receiver is shifted away from the centre of the sample, although the signal strength is slightly higher in the centre. The M-shaped patterns recorded by the receiver located in the centre at the time of the shear wave arrival are particularly misleading from a signal interpretation perspective. They are, however, absent from the signal recorded at one quarter of the diameter, where the arrivals are characterised by clear, sharp peaks that support their unequivocal visual interpretation. Conversely, no significant improvement is identified in the readings of the receiver shifted away from the centre in the lowest frequency configuration, as both amplitude and sharpness of the first arrival signals are similar. No M-shaped patterns are present in any of the configurations.

5. Conclusions

A new method for the optimisation of the receiver's location in bender element experiments is presented in this paper. The research is motivated by experimental evidence that the tip-to-tip transmitter-receiver configuration, by far the most common in laboratory tests using bender elements, does not always endorse the clearest signal corresponding to the arrival of the shear wave. The single most important reason for this issue is the pollution of the output signal with residual compression waves reflected from the lateral boundaries of the sample. The intensity of the compression and shear waves is not uniform throughout the sample, so it may be possible to identify locations where the compression waves are dim, while the shear waves are strong. Such locations would be ideal for the installation of the receiver bender element to endorse a clear interpretation of the output signal, but their identification cannot be made based on experimental observation alone.

Conversely, the hybrid-Trefftz finite elements provide the means for the clear-cut numerical filtration of the compression (or shear) waves from the response of the sample, since the separation of compression and shear approximation functions is inherent to the way the Trefftz basis is constructed. This property enables the construction of compression and shear traces, which are plots of the maximum intensity of the respective waves throughout the sample during the time interval of interest. The analysis of the traces enables the optimisation of the location of the bender element receiver.

Applied to a benchmark bender element test, the procedure reveals that the optimal location of the receiver does not correspond to the centre of the sample. Shifting the receiver bender element away from the tip-to-tip configuration secures a clearer peak in the output signal corresponding to the arrival of the shear wave, while its intensity is not significantly inferior to that obtained in the centre of the sample. This is true for excitation frequencies similar to or higher than the resonant frequency of the coupled bender-soil system. However, shifting the receiver away from the centre of the sample does not significantly improve the quality of the output signal for excitation frequencies much lower than the resonant frequency, because the high intensity zones of the compression and shear traces tend to coincide.

The optimal location of the receiver is problem-dependent. It is strongly affected by the mechanical parameters of the geomaterial and the conditions under which the experiment takes place. However, the procedure described in this paper can be applied to any experimental configuration to better understand the wave propagation patterns and increase the reliability of the experiment. The applicability of the procedure is enhanced by the free online availability of the Trefftz computational platform FreeHyTE, where the results presented in this paper are obtained.

Credit author statement

Ionut Dragos Moldovan: Conceptualization, Methodology, Software, Validation, Investigation, Data curation, Writing – original draft, Writing – review & editing, Visualization, Supervision, Project administration, Funding acquisition. António Gomes Correia: Conceptualization, Methodology, Investigation, Writing – review & editing, Supervision, Project administration, Funding acquisition.

Declaration of competing interest

All authors have participated in (a) conception and design, or analysis and interpretation of the data; (b) drafting the article or revising it critically for important intellectual content; and (c) approval of the final version.

This manuscript has not been submitted to, nor is under review at, another journal or other publishing venue.

The authors have no affiliation with any organization with a direct or indirect financial interest in the subject matter discussed in the manuscript.

Acknowledgements

Appendix A. Supplementary data

Supplementary data to this article can be found online at https://doi.org/10.1016/j.soildyn.2021.106591.

References

[1] Ayala J, Villalobos F, Alvarado G. Study of the elastic shear modulus of bío bío sand using bender elements in an oedometer. Geotech Test J 2017;40(No. 4):673–82.

[2] Molina-Gomez F, Viana da Fonseca A, Ferreira C, Camacho-Tauta J. Dynamic properties of two historically liquefiable sands in the Lisbon area. Soil Dynam Earthq Eng 2020;132:106101.

[3] Alvarado G, Coop MR. On the performance of bender elements in triaxial tests. Geotechnique 2012;62(No. 1):1–17.

[4] Dyvik R, Madshus C. Lab measurements of G_{max} using bender element. In: *Proceedings of the ASCE Convention on Advances in the Art of testing Soils under cyclic conditions*; 1985. p. 186–96.

[5] Santos J, Santos J, Ferreira C, Pereira C, Gomes Correia A. Assessment of shear modulus by different seismic wave-based techniques. In: Rinaldi VA, Zeballos ME, Clariá JJ, editors. Deformation characteristics of geomaterials. IOS Press; 2015. p. 374–81.

[6] Cai Y, Dong Q, Wang J, Gu C, Xu C. Measurement of small strain shear modulus of clean and natural sands in saturated condition using bender element test. Soil Dynam Earthq Eng 2015;76:100–10.

[7] Moldovan ID, Gomes Correia A, Pereira C. Bender-based G_0 measurements: a coupled numerical-experimental approach. *Comp. Geo* 2016;73:24–36.

[8] Arroyo M, Greening PD, Muir Wood D. An estimate of uncertainty in current laboratory pulse test practice. Riv Ital Geotec 2003;1(No. 3):38–56.

[9] Wang YH, Lo KF, Yan WM, Dong XB. Measurement biases in the bender element test. J. Geotech. Geoenviron 2007;133(No. 5):564–74.

[10] Viggiani G, Atkinson JH. Interpretation of bender element tests. Geotechnique 1995;45(No. 1):149–54.

[11] Vilhar G, Jovicic V. Measurement and interpretation of the small strain stiffness of Bostanj silty sand. Acta Geotech. Slov 2009;6(No. 2):57–75.

[12] Camacho-Tauta J, Ali H, Cascante G, da Fonseca AV. Experimental and numerical observations of the frequency-domain method in bender-element testing. J. Geotech. Geoenviron 2017;143(No. 2):04016096.

[13] Ogino T. Travel time observation using numerical simulation of bender element testing in time and frequency domain. Soils Found 2019;59(No. 3):657–70.

[14] Lee J-S, Santamarina J. Bender elements: performance and signal interpretation. J. Geotech. Geoenviron 2005;131(No. 9):1063–70.

[15] Greening P, Nash D. Frequency domain determination of G_0 using bender elements. G*eotech Test J* 2004;27(No.3):288–94.

[16] Moldovan ID, Gomes Correia A. Fixed point automatic interpretation of bender-based G_0 measurements. C*omp. Geo* 2017;89:128–42.

[17] Ingale R, Patel A, Mandal A. Performance analysis of piezoceramic elements in soil: a review. Sensor. Actuat. A-Phys 2017;262:46–63.

[18] Kumar J, Shinde NS. Interpretation of the bender element test results using the sliding Fourier transform method. Can Geotech J 2019;56(No. 12):2004–14.

[19] Moldovan ID, Cao DT, Freitas JAT. Hybrid-Trefftz displacement elements for elastic unsaturated soils. Int J Comput Methods 2014;11(No. 2):1342005.

[20] Freitas JAT, Cismasiu C. Hybrid-Trefftz displacement element for spectral analysis of bounded and unbounded media. Int J Solid Struct 2003;40:671–99.

[21] Freitas JAT, Moldovan ID. Hybrid-Trefftz displacement element for bounded and unbounded poroelastic media. Comput Mech 2011;48:659–73.

[22] Moldovan ID, Cismasiu I. FreeHyTE: a hybrid-Trefftz finite element platform. Adv Eng Software 2018;121:98–119.

[23] Moldovan ID, Climent N, Bendea ED, Cismasiu I, Gomes Correia A. A hybrid-Trefftz finite element platform for solid and porous elastodynamics. Eng Anal Bound Elem 2021;124:155–73.

[24] FreeHyTE release page. https://www.sites.google.com/site/ionutdmoldovan/freehyte. [Accessed 1 July 2020].

[25] Freitas JAT, Moldovan ID, Cismasiu C. Hybrid-Trefftz displacement element for bounded and unbounded poroelastic media. Comput Mech 2011;48:659–73.

[26] Freitas JAT. Mixed finite element solution of time-dependent problems. Comput Methods Appl Mech Eng 2008;197:3657–78.

[27] Yamashita S, Kawaguchi T, Nakata YMT, Fujiwara T, Shibuya S. International parallel test on the measurement of gmax using bender elements. Soils Found 2009; 49(No. 4):631–50.

[28] Biot MA. Theory of propagation of elastic waves in a fluid saturated porous solid. II. Higher frequency range. J Acoust Soc Am 1956;28(No. 2):179–91.

[29] Youn J-U, Choo Y-W, Kim D-S. Measurement of small-strain shear modulus Gmax of dry and saturated sands by bender element, resonant column and torsional shear tests. Can Geotech J 2008;45(No. 10):1426–38.

[30] Li H, Senetakis K. Dynamic properties of polypropylene fibre-reinforced silica quarry sand. Soil Dynam Earthq Eng 2017;100:224–32.

[31] Santamarina JC, Fam MA. Interpretation of bender element tests. Geotechnique 1997;47(No. 4):873–7.